AIAA JOURNAL
Vol. 42, No. 4, April 2004

Skin Friction Measurements for Recirculating Normal-Shock/Boundary-Layer Interaction Control

Yeol Lee*
Hankuk Aviation University, Koyong-Si 412-791, Republic of Korea
and
Everett S. Hafenrichter,† J. Craig Dutton,‡ and Eric Loth§
University of Illinois at Urbana–Champaign, Urbana, Illinois 61801

Skin-friction measurements for a normal-shock/boundary-layer interaction with several recirculating flow control methods have been conducted in a planar Mach 1.4 wind tunnel. The skin friction has been measured along the spanwise centerline and downstream of the interaction using the laser interferometry skin-friction (LISF) technique, which optically detects the rate of thinning of an oil film applied to the test surface. Velocity profiles measured by laser Doppler velocimetry at the same locations as the LISF measurements in the interaction were also used to evaluate the skin friction. Comparison of the two measurement techniques for skin friction is found to show reasonable agreement. Various configurations of the mesoflap arrays of different shapes and thicknesses were examined, and the results were compared to cases of both a solid wall with no control mechanisms and conventional recirculating passive flow control with a porous plate. Of the various mesoflap arrays tested, one mesoflap array provided higher skin friction downstream of the interaction, and as such tends to have better recovery from flow separation. However, all values of skin friction for the mesoflap arrays and the porous plate were found to be lower than for the solid-wall reference case. As such, the flow downstream of these control systems can be more susceptible to separation for this particular condition, although the control systems may reduce viscous drag in external flows.

Introduction

THE interaction of a shock wave with a turbulent boundary layer constitutes one of the fundamental problems of modern internal/external high-speed fluid dynamics. A detailed survey of past work on such interactions has been carried out by Settles and Dolling[1] and Smits and Dussauge.[2] When a shock wave of sufficient strength interacts with the turbulent boundary layer on a solid surface, a complicated separated flow region can be generated, which can typically lead to poor quality of the outgoing boundary layer. In particular, shock/boundary-layer interactions in supersonic engine inlets can cause significant stagnation pressure losses and flow nonuniformities downstream that generally degrade overall engine performance. Traditional flow-control techniques[3,4] have avoided these problems by employing active blowing or bleeding of the boundary layer on the engine inlet, which requires a heavier and more complicated inlet design.

Previous research efforts[5–7] on shock/boundary-layer interaction control have shown that recirculating flow-control techniques employing natural recirculation in a cavity beneath the interaction region through slots or holes can result in positive effects on total pressure recovery. However, the performance of conventional recirculation techniques can deteriorate at off-design conditions, and they can induce the negative impact of a roughened surface on boundary-layer characteristics. Furthermore, the quantitative impact on wall shear stress is not clear because no measurements of the downstream skin friction for such devices have been obtained experimentally.

Recent work[8–11] at the University of Illinois at Urbana–Champaign has shown that a recirculating flow-control system utilizing aeroelastic mesoflaps (flaps of the order of millimeters in length) can produce both better total pressure recovery and decreased boundary-layer thickness downstream of the interaction for some conditions. The concept of this system consists of a matrix of mesoflaps mounted over a cavity that spans the interaction region (Fig. 1). Each flap can deflect aeroelastically upward or downward according to the pressure difference between the cavity below and the flowfield above the flaps, which is associated with the shock structure. The nearly constant cavity pressure lies between the low-pressure upstream of the shock structure and the high-pressure downstream. Therefore, the upstream flaps will deflect upward, allowing mass flow injection into the boundary layer, and the downstream flaps will deflect downward, bleeding off low-momentum fluid from the boundary layer (Fig. 1a). The upstream injection produces multiple leading oblique shocks starting farther upstream than the single oblique leading shock that occurs without the injection. The result is a much larger and more complex lambda–foot shock system. Thus, the major advantages of the aeroelastic mesoflap system can be better total pressure recovery downstream due to the multiple oblique shock interaction (the lambda–foot benefit) and more rapid recovery of the thickened boundary layer due to bleeding downstream of the interaction. Furthermore, because the flaps revert to a nearly smooth solid wall at off-design subsonic conditions (Fig. 1b), there are minimal negative effects of a roughened surface as compared to previous passive flow control systems with holes or slots.

In the present work, further details of this novel flow control mechanism applied to a normal-shock/boundary-layer interaction are investigated, focusing particularly on the skin friction downstream of the interaction. The skin friction is of interest because it bears directly on possible flow separation and the characteristics of boundary-layer recovery from the shock interaction. Previous parametric studies by Inger and Zee[12] of typical blowing and bleeding effects on the skin-friction distribution in a transonic-shock/boundary-layer interaction have identified two competing effects: Blowing decreases skin friction, whereas bleeding increases it. A study by

Received 23 November 2002; revision received 2 May 2003; accepted for publication 8 September 2003.

*Associate Professor, School of Aerospace and Mechanical Engineering. Senior Member AIAA.
†Graduate Research Assistant, Department of Mechanical and Industrial Engineering. Member AIAA.
‡W. Grafton and Lillian B. Wilkins Professor, Department of Mechanical and Industrial Engineering. Associate Fellow AIAA.
§Professor and Willett Faculty Scholar, Department of Aeronautical and Astronautical Engineering. Associate Fellow AIAA.

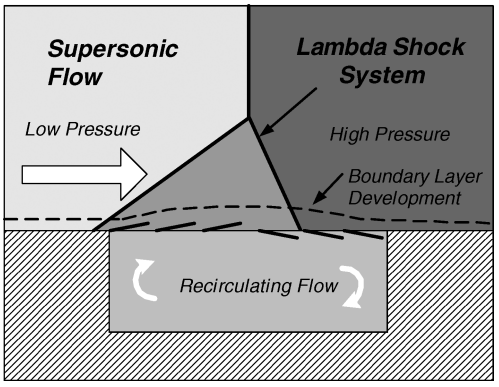

a) Normal-shock/boundary-layer interaction with mesoflap system

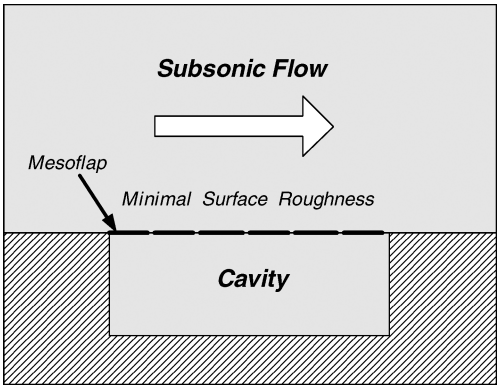

b) Off-design conditions for subsonic flows

Fig. 1 Schematic of concept of the aeroelastic mesoflap system.

Bur et al.[5] of passive flow control utilizing various perforated plates in a transonic interaction has found that the combined blowing–bleeding effect results in an increase of viscous drag. This effect, combined with a substantial reduction of wave drag, caused Bur et al.[5] to conclude that passive flow control utilizing perforated plates can slightly decrease the total drag. However, their conclusions on viscous drag downstream of the interaction were based on information concerning the integral properties of the boundary layer through velocity profile measurements and have not fully clarified the impact on the boundary-layer state. Raghunathan and Mabey[6] and Nagamatsu et al.[7] have also shown similar results of a decrease of total drag in transonic-shock interactions over porous walls; however, they did not clearly identify the distribution of skin friction through the interaction. Furthermore, these previous studies have focused mostly on external flows.

The present research program provides the first set of wall-skin-friction measurements using laser interferometry for shock/boundary-layer interaction control with recirculating transpiration. Various configurations of the mesoflap arrays with different shapes and thicknesses have been examined. The results are compared to both the cases of a solid wall with no control mechanisms and conventional passive flow control with a porous plate. Velocity profiles of the boundary layer downstream of the interaction, measured by laser Doppler velocimetry (LDV), are also utilized to evaluate the skin friction, and the results of the two methods are compared.

The present experimental results provide an improved understanding of wall-skin-friction recovery in such shock/boundary-layer interactions with flow control and also provide high-quality data for computational fluid dynamics code validation.

Experimental Methods

Flow Model and Test Conditions

All experiments were conducted in the Gas Dynamics Laboratory at the University of Illinois at Urbana–Champaign. Figure 2 is a schematic diagram of the test section, in which the region of

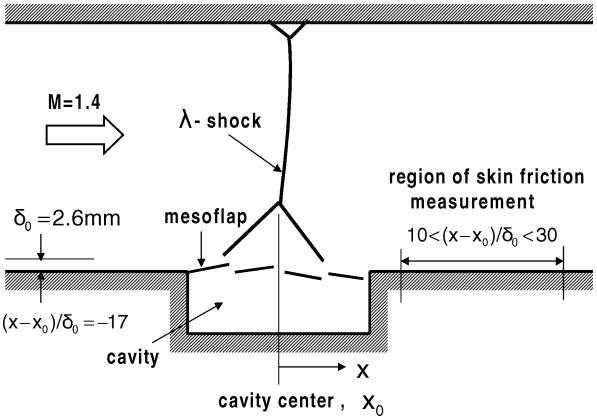

Fig. 2 Schematic diagram of the test section.

the skin-friction measurements and other features are shown. A converging–diverging nozzle block in the blowdown-type normal shock facility, designed using a method of characteristics design code, provides uniform Mach 1.4 flow, with a unit Reynolds number of 30×10^6 m^{-1} to the 50.8×50.8 mm test section. The position of the normal-shock wave can be controlled by varying the tunnel stagnation pressure using a Fisher TL101 process controller. The backpressure remains constant at a level slightly higher than atmospheric pressure, due to losses in the exhaust ductwork. The tunnel stagnation pressure necessary to position the shock wave above the center of the flap array varies slightly, depending on the test conditions and the particular mesoflap array being studied, but is usually around 210 kPa. The tunnel stagnation pressure can be maintained to within $\pm 1.5\%$ (95% confidence level, i.e., $\pm$two standard deviations) of the target value, which holds the position of the shock wave constant within ± 3 mm (in the streamwise direction) above the center of the mesoflap array. The stagnation temperature remains almost constant throughout the experiments at about 300 K.

The incoming mean velocity profile measured at 17 incoming boundary-layer thicknesses δ_0 upstream of the location of the main inviscid-shock wave shows the characteristics of a fully developed turbulent boundary layer with a thickness of 2.6 mm. Other integral properties of the boundary layer at the same location, such as the incompressible displacement thickness and the incompressible momentum thickness, are 0.356 and 0.203 mm, respectively, and the freestream velocity is 405 m/s. Further detailed information for the incoming boundary layer, including the mean velocity profile, is presented in Ref. 10.

The cavity in the present experiments is located slightly downstream of the end of the diverging section of the nozzle, spans the entire 50.8 mm width of the test section, and is 44.5 mm long and 19.1 mm deep.

Figures 3a–3c show schematic diagrams of the mesoflap arrays examined in the present experiments. The flow direction is from left to right in Fig. 3. Each mesoflap array tested in the present work is manufactured from a superelastic nickel–titanium alloy (nitinol) or aluminum and measures 50.8 mm in width and 57.2 mm in length. Six-flap and four-flap arrays of a conventional rectangular shape (Figs. 3a and 3b; nitinol) and S-shaped arrays (Fig. 3c; aluminum) of different thicknesses have been investigated to achieve various levels of flap deflections and to examine their ability to control the interactions. The maximum porosity of these mesoflaps in the undeformed state is approximately 3%. Each mesoflap array has several new features as compared to previous designs, such as rounded corners and stress-relief holes, to achieve more mechanical robustness. More detailed descriptions of the manufacture and installation of the flap arrays in the test section may be found in Ref. 10.

Figure 3d is a schematic of a conventional passive control device that was examined, a macroporous plate (aluminum) machined with a staggered array of normal holes of diameter 1.3 mm with a spacing yielding a porosity of 5%, which is larger than that for the mesoflaps in the undeformed state. The term macroporous refers to the hole diameters, which are on the order of the displacement thickness of

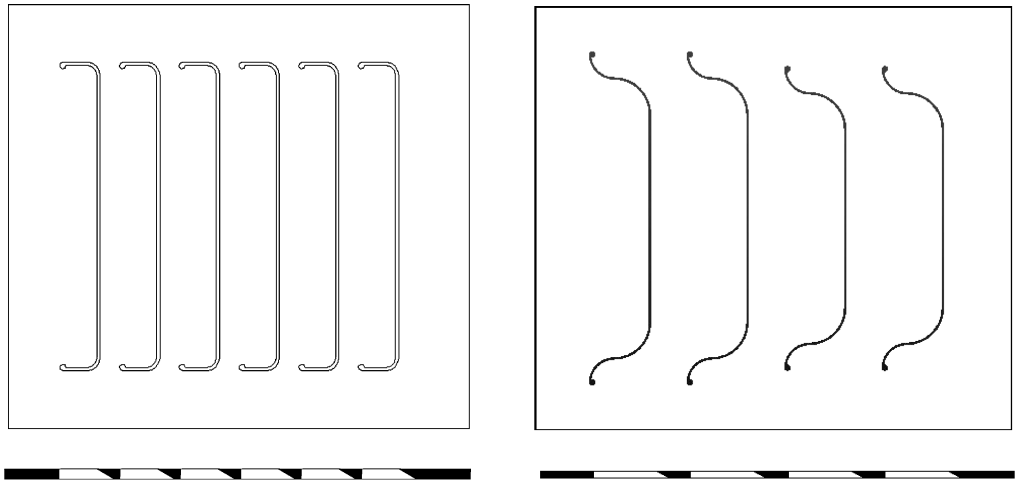

a) Six-flap mesoflap array (nitinol)

c) Four-flap S-shaped mesoflap array (aluminum)

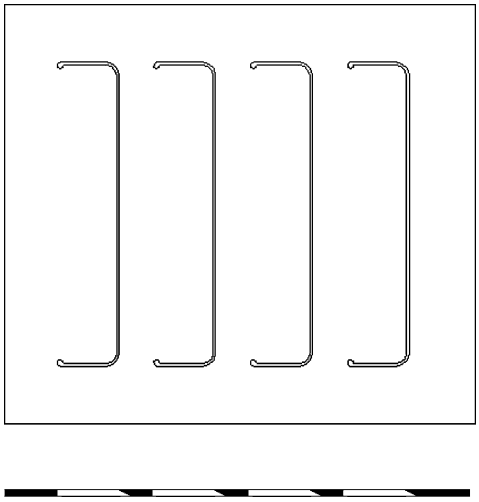

b) Four-flap mesoflap array (nitinol)

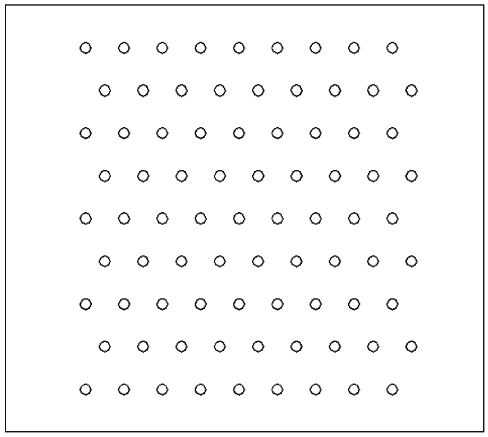

d) Conventional macroporous plate

Fig. 3 Top view of mesoflap arrays, with stringer profiles below, and macroporous plate.

the incoming boundary layer, as opposed to microporous plates for which the hole diameters are on the order of tens of micrometers.

Measurement Techniques

Various diagnostic techniques have been employed to quantify the performance of the mesoflap control system. These methods include static pressure measurements, measurements of steady/unsteady total pressure recovery, LDV velocity measurements, shadowgraphs, oil-streak surface flow visualization, and measurements of skin friction. A brief description of the skin-friction measurement methodology is given herein, whereas the other techniques are explained in detail in Refs. 9 and 10.

Skin-friction measurements were made using the laser interferometry skin-friction (LISF) meter, which optically detects the rate of thinning of an oil film applied to the test surface. Under proper conditions, the skin friction can be obtained nonintrusively using this technique without any reference to the properties of the overlying boundary layer.

The LISF meter was first developed by Tanner and Blows[13] and has been successfully implemented in highly compressible flows.[14,15] A schematic diagram of the LISF setup employed for the present experiments is shown in Fig. 4. The beam from a 5-mW He–Ne laser is focused to form a spot of less than 400-μm diam on the test area. During the tunnel runs, a thin film of silicone oil (Dow–Corning Fluids 200; kinematic viscosity $\nu = 500$ cS) applied to the test surface is sheared by the flow and is thinned. Both the surface of the oil film and the polished stainless steel test surface beneath it reflect the incident laser beam. These reflections produce interference between the two reflected beams, which is directed to a photodetector through optical components. The photodetector senses a time-varying light intensity due to the constructive and destructive interference between the two reflected beams. The signal from the photodetector is then low-pass filtered (20-Hz cutoff) to remove high-frequency noise and is digitally recorded by a data acquisition system at a 100-Hz sampling rate. The entire LISF instrument is pedestal mounted on an optical breadboard that is independent of the wind tunnel itself to avoid vibrations from the tunnel, which were found to be negligible.

The time variation of the test surface temperature, which results in the variation of oil viscosity, is accounted for by installing three fast-response miniature thermocouples (Omega; KMQSS-040-G-2) just beneath the test surface and by assuming that the temperature of the oil film is identical to the surface temperature. The surface temperature of the test region generally quickly increases during tunnel startup and then slowly decreases for the rest of the test period. The amount of temperature drop in the test region during a run depends on the specific flow conditions, but is typically less than 1°C. The measured test surface temperature is then substituted into the known viscosity–temperature relationship[16] provided by the manufacturer of the oil to determine the oil viscosity. The sensitivity of the oil viscosity to temperature variation is less than 2%/°C.

A telemicroscope mounted on a microtraverse is used to measure the distance from the oil-film leading edge to the center of the beam

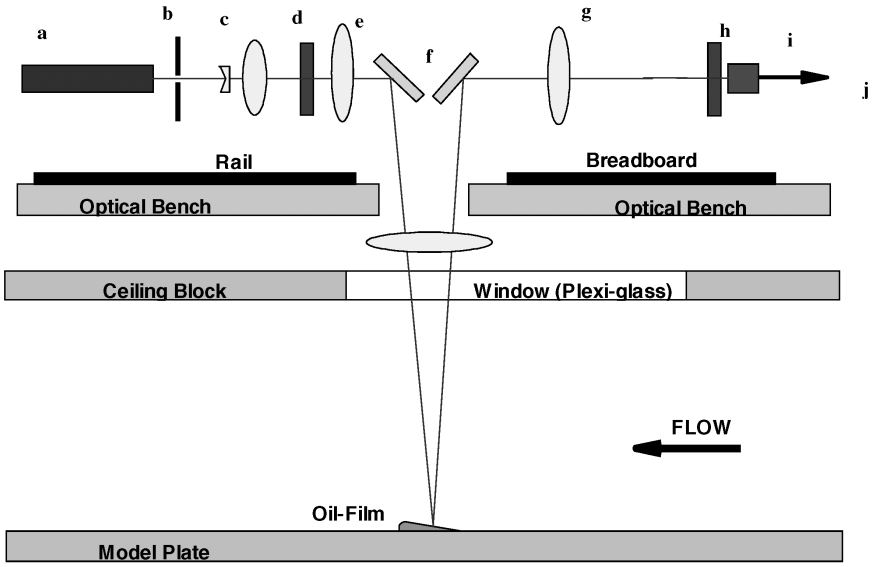

Fig. 4 Schematic of LISF setup: a, He–Ne laser; b, iris; c, beam expander; d, ND filter (50%); e, lens; f, mirrors; g, lens; h, wavelength filter; i, photo-detector; and j, data acqusition system (low-pass filter/oscilloscope).

spot. Because the accuracy of this distance directly affects the final quality of the skin-friction measurement, it is carefully measured with an error of less than $\pm 1\%$ (95% confidence level). The distance is typically in the range of $3.0 \sim 3.5$ mm for the present experiments.

During tunnel runs, surface wave phenomena on the oil film can induce serious limitations on the usefulness of the LISF data, especially in high-speed flows. To reduce the undesired effects of these weak waves on the surface of the oil film, a prethinning process of the film before tunnel startup is required. This is done by placing the edge of a thin plastic film over the oil that was partially deposited on masking tape and by wiping it in the downstream direction. The masking tape is then removed from the test surface before the tunnel starts. This procedure provides a well-defined oil-film leading edge, and reduces the period of noisy fringe signals that occurs during the transient period of tunnel startup.

To obtain a tightly focused beam on the test surface for good signal-to-noise ratio, a beam expander is utilized. The angle between the incident beam and the reflected beam from the test surface should also be kept as small as possible and is about 1 deg for the present setup.

LISF Data Reduction

The analytical phase equation utilized in the LISF technique is described briefly. A more detailed account of the LISF data-reduction procedure is given by Kim and Settles[14] and Garrison.[15] The phase difference δ between the two reflected beams, one from the surface of the oil film and the other from the test surface, is given by[15]

$$\delta = 4\pi n_f S X \cos\theta_t \Big/ \lambda\tau \int_0^{t^*} \frac{\mathrm{d}t^*}{\mu} \tag{1}$$

where n_f and μ are the refractive index and viscosity of the oil, respectively. Also, X in Eq. (1) is the distance between the oil leading edge and the beam spot, and θ_t is the angle between the incident beam (wavelength λ) and the reflected beam from the oil-film surface. Furthermore t^* is the oil flow time, and τ is the wall shear stress of interest. S is a correction factor for three-dimensional flows in regions where the surface streamlines are not parallel. For the present case, S is assumed to be unity. The LISF signal from the photodetector is utilized to extract information on the phase difference δ in Eq. (1).

Garrison[15] modified the preceding analytical phase equation and provided enhanced features of an LISF data-reduction procedure that utilized the entire LISF signal to determine the wall shear stress.

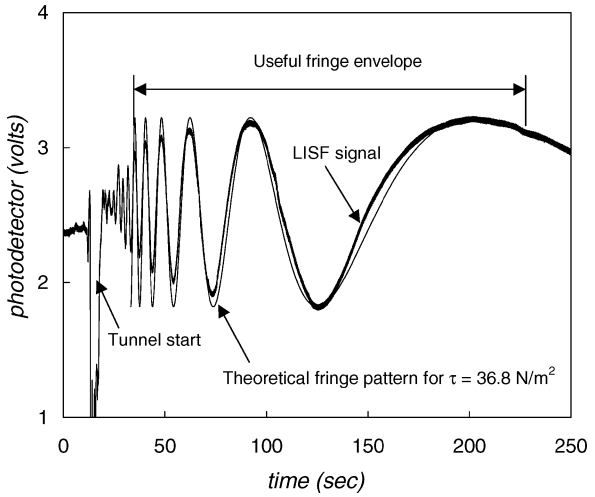

Fig. 5 Typical pattern of photodetector signal in the LISF measurements; solid-wall interaction, measurement location $(x - x_0)/\delta_0 = 14.2$.

In his data reduction procedure, the value of shear stress is determined by taking cross correlations between the actual LISF fringe signal and theoretical fringe patterns for guessed shear stresses, with the measured value of shear stress being the value that yields the maximum correlation. The present skin-friction measurement technique employs Garrison's data-reduction method.

In Fig. 5, a typical fringe record from the LISF measurements downstream of the normal shock/boundary-layer interaction for the solid-wall case [measurement location $(x - x_0)/\delta_0 = 14.2$] is compared with a theoretical fringe pattern for a certain value of wall shear stress determined by the analytical phase equation. The streamwise location, $(x - x_0)/\delta_0$, is nondimensionalized by the incoming boundary-layer thickness, $\delta_0 = 2.6$ mm, and is defined to be zero at the cavity center x_0, that is, at the location of the main inviscid shock wave (Fig. 2). Because the oil film over the test area is initially not thin enough even after the prethinning process, the signal just after tunnel startup is shown to suffer from surface-wave distortion, resulting in scattering of the laser beam and causing an abrupt decrease of signal intensity. The duration of this unusable portion of the fringe pattern is believed to be partially dependent on the initial oil-film thickness and the distance between the oil-film

leading edge and the laser beam spot. Soon after startup, these negative surface-wave effects are alleviated, and typically 5–19 usable fringes, depending on the specific flow conditions, are obtained. Near the end of a tunnel run, the oil film can become very thin. At this point, the oil film does not change its thickness significantly, the resultant interference signal broadens, and additional distortion can occur. Thus, the initial and final segments of the fringe record are discarded in the data-reduction procedure. Also note in Fig. 5 that the rms noise level in the fringe signal does not change significantly before and during the test. Furthermore, the frequency range of interest of the signal is much lower (0.1–0.01 Hz) than any higher frequency noise associated with tunnel and flow vibrations, and the high-frequency noise was also eliminated by a low-pass filter.

In Fig. 5, the typical period of the useful fringe envelope is shown to be about 200 s, and 12 usable fringe peaks are observed in this particular envelope. The raw data of the useful fringe envelope are smoothed before locating the fringe peaks, and the phase information of the fringe peaks is utilized to construct an analytical expression of phase variation for a guessed shear stress. Finally, the value of shear stress is determined by taking the cross correlation between the actual LISF signal and the analytical phase variation, the final value being that which yields the maximum correlation between the two data sets. In Fig. 5, the analytical phase signal for the estimate of wall shear stress of 36.8 N/m^2 is the case of maximum correlation with the experimental LISF signal and is the value returned by the data-reduction procedure.

Overall Oil-Surface Fringe Patterns

Overall surface fringe patterns can provide a quick, qualitative indication of the spatial distribution of wall shear stress over a certain region of interest. To obtain such patterns, several drops of the silicone oil (500 cS) are applied over a certain region of the interaction and are wiped in the downstream direction by a plastic film. Thus, a thin oil film is created over the region with a near-uniform initial thickness. During a wind-tunnel run (approximately 150 s), the two-dimensional interference fringe pattern forms naturally because of the wall shear stress variation imposed by the flow. Thus, a spatially varying fringe spacing is generated, which depends on the local shear stress level. Such visible patterns, which can be photographed in white light, provide qualitative information concerning the wall shear stress distribution over a region of the shock/boundary-layer interaction. Representative results of this method are presented and discussed briefly.

Results and Discussion

Flow Visualization

Figure 6a shows a shadowgraph photograph of the reference case, that is, the normal-shock interaction with the solid wall. Typical features of a normal-shock/boundary-layer interaction are clear: a short leading oblique shock wave and a nearly normal trailing shock wave, resulting in the familiar lambda-shock structure. Figure 6b shows the interaction of the normal-shock wave with a mesoflap array (four-flap, flap thickness $t = 191$ μm; Fig. 3b). Compared to the typical normal-shock interaction shown in Fig. 6a, the interaction with the mesoflap array consists of a larger lambda-shock shape with a series of weak oblique shock waves upstream and a terminating nearly normal-trailing-shock wave. A secondary normal-shock wave also can be observed downstream of the interaction, which is stronger than the weak waves seen for the solid-wall case. This secondary wave is presumably evidence of the mesoflaps bleeding flow into the cavity in the downstream half of the array, which should cause a stronger acceleration of the flow downstream. Velocity profile measurements[10] downstream of the interaction have also shown this local reacceleration. From Fig. 6, it is evident that the mesoflap control system can increase overall stagnation pressure recovery for internal flows from the lambda–foot benefit of the multiple leading oblique shocks.

LISF Measurement Accuracy

A calibration of the present LISF instrument was performed for a zero pressure gradient (no shock interactions) two-dimensional

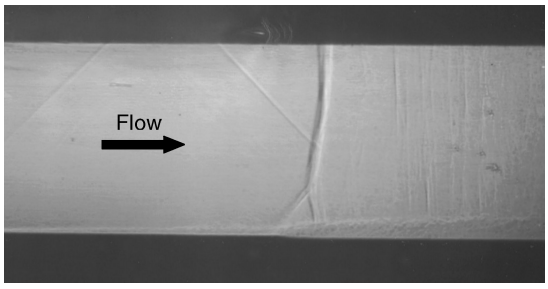

a) Solid-wall reference case

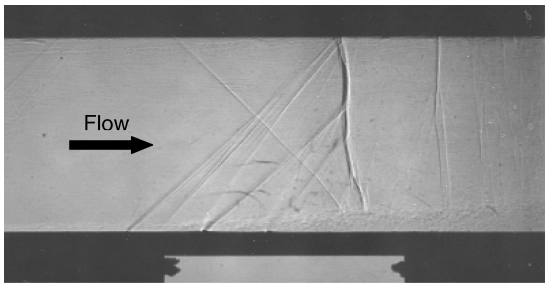

b) Four-flap 191-μm mesoflap array (nitinol)

Fig. 6 Comparison of shadowgraph visualizations for solid wall and mesoflap array.

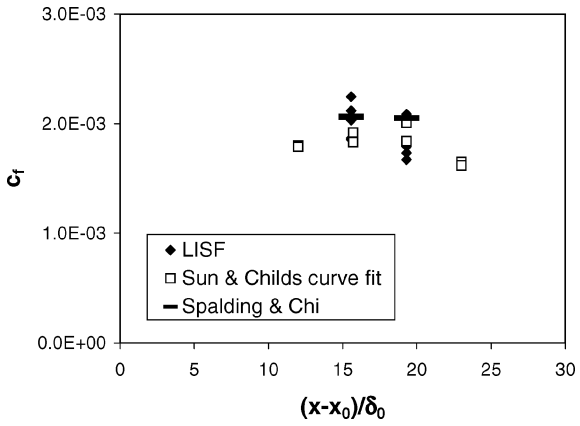

Fig. 7 Comparison of LISF measurements with Spalding and Chi[17] prediction and Sun and Childs[18] curve fit for zero pressure gradient turbulent boundary layer.

compressible turbulent boundary layer. This flow condition was achieved by swallowing the normal-shock wave far downstream of the test section by increasing the tunnel stagnation pressure, resulting in a well-defined two-dimensional turbulent boundary layer in the test area. Five test runs for skin-friction measurement at each of two streamwise locations were executed to check repeatability. Except for the overall surface fringe patterns for qualitative flow visualization, the quantitative LISF measurements for all cases were made on the spanwise centerline of the facility. The results of the skin-friction measurements were compared to the analytical expression suggested by Spalding and Chi.[17] The results of the LISF measurements were also compared to the value determined by a Sun and Childs[18] curve fit to velocity profile measurements by LDV at the same locations for identical flow conditions.

Figure 7 summarizes the results of the calibration and repeatability of the present LISF measurements of the skin-friction coefficient, c_f. In Fig. 7, the LISF results at the two different locations match with the predictions of Spalding and Chi's method[17] within about $\pm 7\%$ in an average sense. In the comparison with the Sun and Childs curve fit to the velocity profile data, the maximum deviation of the LISF results is of the order of $\pm 10\%$. The repeatability of the LISF data is about $\pm 14\%$, that is, $\pm$ two standard deviations, at the first

measurement location and about ±18%, that is, ± two standard deviations, at the second measurement location. Previous studies[14,15] utilizing a similar setup of LISF instrumentation have also shown measurement accuracy in the same range. All of these results demonstrate that the present LISF technique can reasonably measure skin friction in a highly compressible flat plate, zero pressure gradient turbulent boundary layer, at least to an accuracy of about ±16%, that is, ±two standard deviations. For the region downstream of the shock/boundary-layer interactions, which is possibly associated with streamwise pressure gradients and/or flow three dimensionality, the present measurement accuracy could be less. However, to the authors' knowledge, no calibration standard currently exists with which to judge the absolute accuracy of LISF measurements in such a complex flow.

Velocity Profile Method for the Interactions

The LISF data for the solid-wall interaction have been compared to experimental data by Kooi,[19] which has the closest flow conditions to the present solid-wall interaction among many previous studies. The comparison revealed that Kooi's skin-friction data were more than 50% higher than the present LISF data, but with a similar pattern of streamwise variation.

Further estimation of skin friction from velocity profile data obtained for identical test condition as the current solid-wall interaction has, thus, been obtained. The velocity profile of the outgoing boundary layer for the present study was obtained by a one-component LDV setup at four locations downstream of the interaction, and the skin friction was evaluated by the Sun and Childs curve-fit procedure.[18] Comparison of these results with the LISF measurements (three to four measurements per location) is shown in Fig. 8. The repeatability of the LISF data was found to be within $\pm 4 \sim 16\%$, (± two standard deviations) of the mean value at all locations. Because of the earlier described unsteady motion of the main inviscid shock (±3 mm in the streamwise direction) over the mesoflap array, there could be an uncertainty in the streamwise measurement location with respect to the inviscid shock position, which corresponds to approximately $(x - x_0)/\delta_0 = \pm 1.2$. This uncertainty of the measurement location with respect to the shock position is shown by placing horizontal uncertainty bars in Fig. 8.

The effect of slightly different Reynolds numbers of the incoming flow on the solid–wall interaction is also shown in Fig. 8. Obviously, the difference in Reynolds numbers of the incoming flow does not have any noticeable effects on the c_f variation for the solid wall, as measured by LISF. From Fig. 8, it is seen that the skin friction increases almost linearly downstream of the interaction, and its value more than doubles through the short distance of $12\delta_0$ (= 31 mm). Thus, the boundary layer recovers relatively rapidly from the shock interaction.

In Fig. 8, the agreement between the LISF and the velocity-profile results is seen to be reasonable. However, linear empirical curve fits

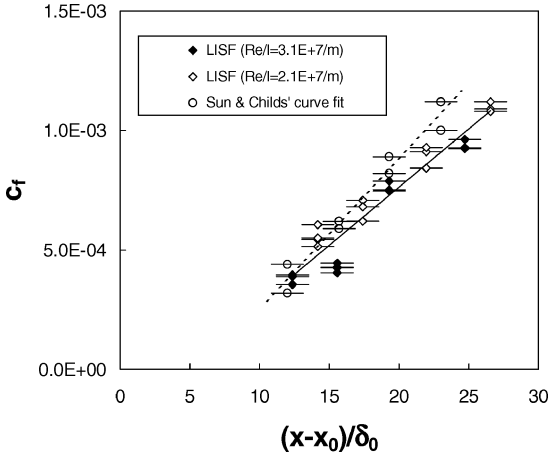

Fig. 8 Comparison of the results of Sun and Childs[18] curve fit with LISF measurements for the solid-wall case.

to the LISF and the Sun and Childs[18] data points in Fig. 8 show that the skin friction determined from the velocity profile method has a slightly steeper slope with respect to downstream distance, as compared to the LISF results.

Note that maximum spatial resolution near the wall in the velocity measurements has been achieved, with the first measurement position located 0.2 mm from the wall and with a traverse spacing between the measurements of 0.2 mm. However, such fine spatial resolution of the first LDV measurement location of 0.2 mm from the wall is found to lie in the range of y^+ from 50 to 100 depending on the flow conditions ($y^+ = u^* y/\nu_f$, where u^*, y, and ν_f are friction velocity, distance from the wall, and kinematic viscosity of the flow, respectively), which is still relatively far from the wall in dimensionless wall units. The repeatability of the LDV measurements was also checked and showed highly consistent results with a slight divergence of the data near the wall. This slight divergence is presumed to be because the positional uncertainties of the LDV probe volume may not be negligible near the wall inasmuch as the wall is difficult to locate exactly with the LDV setup. More detailed information on the LDV setup may be found in Ref. 20.

Further comparisons between the results of the LISF measurements and the velocity profile method for various configurations of the mesoflap flow-control system have also been obtained. These include rectangular-shaped six- and four-flap arrays of different thicknesses (Figs. 3a and 3b) and the conventional macroporous plate (Fig. 3d). In Fig. 9, the skin-friction coefficients estimated from the velocity profile data for those cases are compared with the LISF results. Note that the curve fit of the LISF skin friction data shown in Fig. 8 (solid-wall case) is replotted for comparison purposes in Fig. 9. Uncertainty bars for the streamwise measurement locations with respect to the shock position are also shown. Again, for these cases of the mesoflap interaction, the agreement between the two results from the different measurement techniques is generally reasonable. From Fig. 9, the results of the velocity profile method, as well as the LISF measurements, show that the skin friction for the mesoflap arrays (Figs. 9a–9c) is lower than for the solid-wall reference case. In addition, the skin friction for conventional passive flow control using the macroporous plate is the lowest of all of the cases (Fig. 9d).

Similar trends in comparison between the results of the LISF and the velocity profile method for the solid wall (in Fig. 8) are observed again in Fig. 9, which is that the skin friction determined from the velocity profile method has a slightly steeper slope with respect to downstream distance as compared to the LISF results. The specific reason for this is not clear at the present time. However, it is possible that the present velocity profile data for the mesoflap interactions, which are measured up to 9.2 mm from the wall, may not cover the entire boundary layer, especially far downstream of the interactions (third and fourth measurement locations in the streamwise direction). A slightly underestimated boundary-layer thickness at those locations in the curve-fit method will result in an overestimated value of skin friction, and thus, the difference between skin-friction values from the two techniques will be larger with increasing streamwise distance from the interaction. Better agreement between the two techniques for the macroporous plate (Fig. 9d) is presumed to be due to better coverage of the entire boundary layer in the LDV measurements for the case.

Variations of Skin Friction for the Mesoflap Interactions

Figure 10 shows a comparison of the variation of skin-friction coefficient measured by LISF for the solid-wall interaction with the case of the conventional macroporous plate. The variation of skin friction for the case of the macroporous plate shows a similar linear pattern of the same approximate slope as for the solid-wall case, but with lower values. During the experiments with the macroporous plate, it was found that the main inviscid shock wave tended to stand slightly downstream of the center of the cavity, and this more downstream shock position and the separation bubble behind it seemed to introduce a delay of the boundary layer's development downstream of the interaction. Note that in Figs. 11 and 12, which present the LISF skin-friction measurements for the mesoflap arrays, the linear

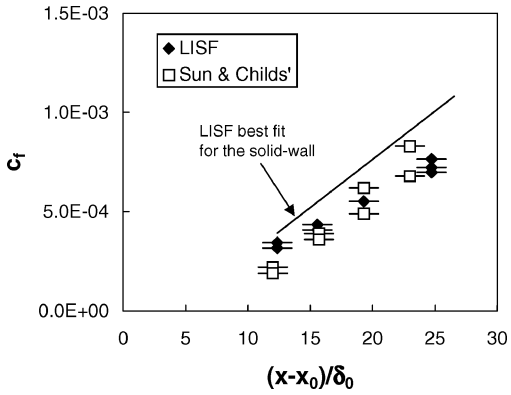

a) 191-μm, four-flap mesoflap array

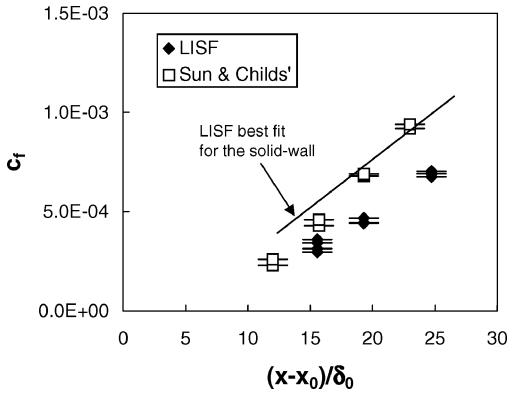

c) 102-μm, six-flap mesoflap array

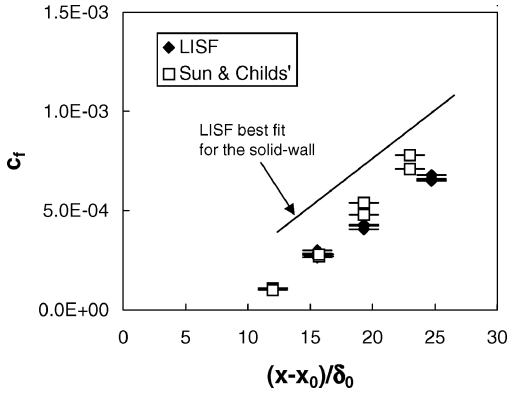

b) 229-μm, four-flap mesoflap array

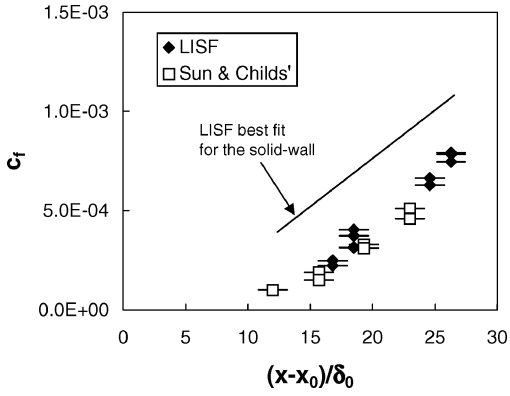

d) Conventional macroporous plate

Fig. 9 Comparison of skin friction determined by velocity profiles with the LISF results.

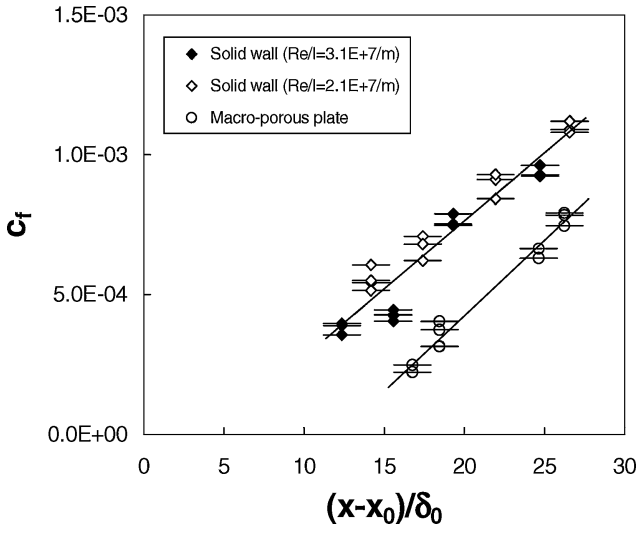

Fig. 10 Comparison of skin friction for the solid-wall and the macroporous plate.

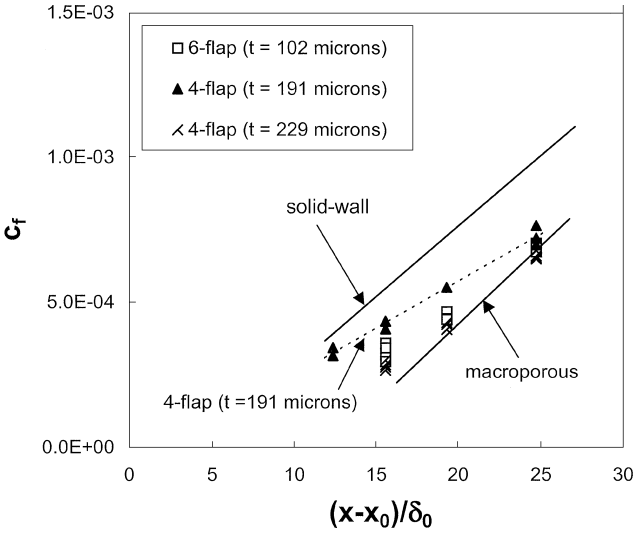

Fig. 11 Comparison of c_f variation for conventional mesoflaps of different thicknesses with the solid-wall case and macroporous plate.

empirical curve fits to the solid wall and macroporous plate data points of Fig. 10 are replotted for comparison purposes.

In Fig. 11, the centerline variations of c_f downstream of the shock/boundary-layer interaction for three different conventional mesoflap arrays [six-flap 102-μm thickness, four-flap 191-μm thickness, and four-flap 229-μm thickness array (Figs. 3a and 3b)] are compared with the solid-wall reference case and the macroporous plate linear curve fits. In Figs. 11 and 12, the streamwise uncertainty bars shown in Figs. 8–10 have been omitted for clarity. In Fig. 11, for all flap array cases, it is observed that skin friction increases in the downstream direction, as the boundary layer recovers from the shock-induced separation. Also note that the skin friction for all cases of the mesoflap arrays is lower than for the solid-wall reference case but higher than for the macroporous plate, that is, the data tend to be bounded by the two extremes. This result suggests that the boundary layer downstream of the mesoflap arrays at the centerline will be more susceptible to boundary-layer separation than for the solid wall, but less susceptible than for the macroporous plate. However, the reduced skin friction indicates that the mesoflap system may have the capability to reduce viscous drag if the system is employed in an external flow such as that over transonic airfoils.

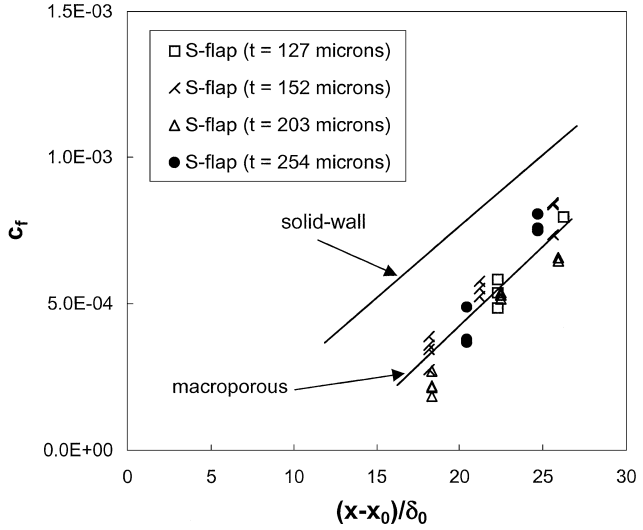

Fig. 12 Comparison of c_f variation for the S-shaped mesoflaps of different thicknesses with the solid-wall case and macroporous plate.

Among the three different mesoflap arrays considered in Fig. 11, the 191-μm, four-flap array shows a larger value of skin friction compared to the other two cases. This is especially true of the skin-friction measurement at the first location, $(x - x_0)/\delta_0 = 12.4$, where c_f could not be obtained for the other two mesoflap cases. It was observed that the oil film did not move downstream and did not get thinner with time for those two cases, which suggests a separation bubble beneath the shock structure that extended to this location for these two mesoflap arrays. Velocity profile measurements by LDV at the same location have also shown a velocity deficit near the wall for the 102-μm, six-flap case and have reconfirmed the present skin-friction measurements. It also appears that the skin-friction values of all three mesoflap array cases asymptotically approach each other downstream. Streamwise static pressure measurements[10] in the same region have shown a similar trend.

Figure 12 shows a comparison of the c_f variation for the S-shaped mesoflaps [four flaps, aluminum (Fig. 3c)] of different thicknesses with the cases of the solid-wall and macroporous plate. Overall, the macroporous plate and S-shaped mesoflaps provide similar variations of skin friction, and c_f is lower than for the solid-wall case. Among the different thicknesses of S-shaped flaps, the 203-μm flap array shows the lowest value of c_f and the 152-μm flap array shows relatively higher values of c_f; however, the differences between these cases lie within the uncertainty level of the measurements.

When Figs. 11 and 12 are considered together, it is apparent that the one particular flap array (four-flap conventional mesoflap array, $t = 191$ μm) that has a higher skin friction downstream of the interaction indicates the ability to provide better recovery of the boundary layer from separation, compared to the other flap arrays. Pressure data and velocity profile measurements[10] by LDV have also demonstrated that this specific mesoflap array has the best improvement in total pressure recovery while producing a slightly reduced momentum thickness downstream of the interaction compared to the solid-wall interaction case. Thus, it may be possible for mesoflap systems to decrease both wave drag and viscous drag under certain conditions. In addition, the results suggest that good stagnation pressure performance for a particular mesoflap configuration tends to be related to higher boundary-layer fullness, that is, higher skin friction, such that these two seemingly separate aspects of performance may be closely coupled and may, thus, be a result of the overall aerodynamic efficiency of the flow control system.

Overall Oil-Surface Fringe Patterns

In Fig. 13, the overall oil-surface fringe patterns for the interaction of the solid wall and the S-shaped mesoflap are compared. In Fig. 13a, which shows the fringe pattern for the case of the solid wall [oil-film leading edge located at $(x - x_0)/\delta_0 = 13.5$], a modest spanwise variation in the fringe pattern is observed, with two

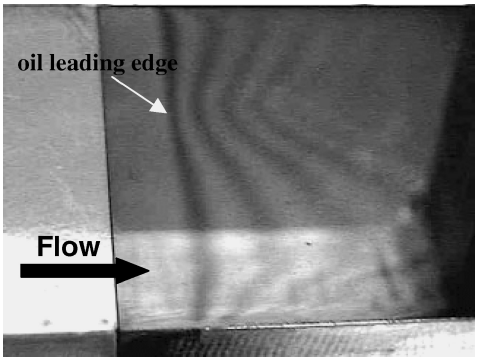

a) Solid wall

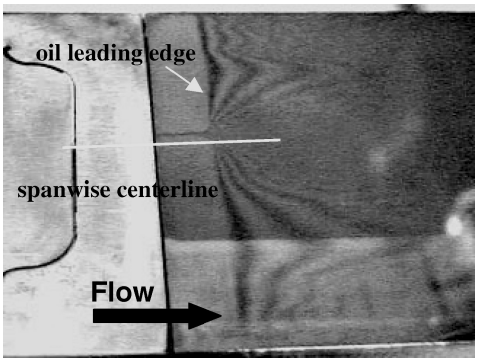

b) S-shaped mesoflap (four flap, $t = 152$ μm)

Fig. 13 Overall oil surface fringe patterns for the solid-wall and the mesoflap interactions: oil leading edge located at $(x - x_0)/\delta_0 = 13.5$.

fringe peaks indicating higher shear stress levels toward the edges of the domain. A region of closer fringe spacing related to lower shear stress is also shown near the spanwise centerline. As the observation region was moved downstream, the trend of the spanwise variation in the fringe pattern was reduced and showed nearly two-dimensional characteristics.

In Fig. 13b, which shows the case of the S-shaped mesoflap array ($t = 152$ μm) for the identical region, more substantial spanwise variation is observed as compared to that seen for the solid-wall case. The fringe pattern is slightly asymmetric about the spanwise centerline. In particular, two strong fringe peaks in the fringe pattern, which are aligned immediately downstream of the corners of the S-shaped flaps, are clearly observed in Fig. 13b. A region of very low shear stress exists near the centerline, which indicates that the separation bubble behind the shock structure is formed in a narrow region near the centerline. As the observation region was moved downstream, the trend of reduced spanwise variation in the fringe pattern was again noticed and demonstrated nearly two-dimensional characteristics. It has also been found that the different shapes and thicknesses of the flap arrays do not show any substantial changes in the global features of the fringe pattern and that the results for the macroporous plate are also qualitatively similar for the overall fringe pattern seen in Fig. 13b.

From Fig. 13, it appears possible that the mesoflaps could produce stronger three-dimensional effects immediately downstream of the interaction as compared to the solid-wall case, and these three-dimensional effects could be partially responsible for the present differences between the LISF and velocity profile measurements of skin friction. Furthermore, the degree of three dimensionality could be different for various mesoflap configurations, and thus, the present comparisons between different flow control devices could be blurred by varying degrees of three dimensionality. Unfortunately, no quantitative information on the spanwise variation of skin friction downstream of the interaction is currently available; the flow three dimensionality is a subject of currently ongoing work. However, farther downstream, the level of three dimensionality is substantially diminished, and comparisons of the measurements at the centerline far downstream of the interactions should be valid. In this case, the

centerline shear stress is expected to be the minimum shear stress observed at a given location downstream of the mesoflaps, that is, the already reported quantitative LISF shear stress values are expect to give a lower bound for the mesoflap shear stress.

Conclusions

Skin-friction measurements along the spanwise centerline for a normal-shock/boundary-layer interaction with an aeroelastic mesoflap flow-control method have been conducted in a planar Mach 1.4 wind tunnel. Various configurations of the mesoflap arrays have been examined, and the results are compared to the cases of a solid-wall and macroporous plate control. One particular conventional mesoflap array (191-μm, four flaps, nitinol) is found to have a higher skin-friction distribution downstream of the interaction compared to other flap arrays, which is assumed to imply better boundary-layer recovery from the shock-induced separation. Interestingly, for this flow condition, this flap array had previously been found to give the highest stagnation pressure recovery as compared to all other flap arrays and the solid-wall case. It is also found that all of the present mesoflap systems tend to have reduced centerline skin friction downstream of the interaction as compared to the solid-wall case, which may indicate the increase of susceptibility to flow separation. The skin-friction coefficient was found to be higher than or equal to that of the macroprous plate for all cases of the mesoflap arrays. The mesoflap system may also be capable of simultaneously reducing wave drag and viscous drag in normal-shock/boundary-layer interactions, which can be important for external flow configurations such as transonic airfoils. The estimation of skin friction from velocity profile data using the Sun and Childs curve-fit method shows generally reasonable agreement with the LISF results. Overall oil-surface fringe patterns immediately downstream of the shock interactions have shown relatively strong spanwise variation in the fringe patterns, which could indicate the three-dimensional nature of the current normal-shock/boundary-layer interaction in this region with and without flow control. Farther downstream, however, the surface fringe patterns are approximately two dimensional.

Acknowledgments

Funding for this work was provided by the Defense Advanced Research Projects Agency under Contract F49620-98-1-0490 with Rich Wlezien as Technical Monitor. We gratefully acknowledge the assistance of Timothy J. Garrison in conducting the present research. He provided a new data reduction code and invaluable advice on the setup of the present LISF instruments. We further appreciate the assistance of Martin Orphanides, Karthik Srinivasan, and Michael Rynne with the experiments.

References

[1]Settles, G. S., and Dolling, D. S., "Swept Shock Wave/Boundary-Layer Interactions," *Tactical Missile Aerodynamics*, edited by M. Hemsch and J. Nielsen, Vol. 104, Progress in Astronautics and Aeronautics, AIAA, New York, 1986, pp. 297–379.

[2]Smits, A. J., and Dussauge, J. P., *Turbulent Shear Layers in Supersonic Flow*, American Inst. of Physics, Springer-Verlag, New York, 1996, Chap. 10.

[3]Delery, J. M., "Shock Wave/Turbulent Boundary Layer Interaction and Its Control," *Progress in Aerospace Sciences*, Vol. 22, No. 4, 1985, pp. 209–280.

[4]Gridley, M. C., and Walker, S. H., "Advanced Aero-Engine Concepts and Controls," CP-572, AGARD, 1996.

[5]Bur, R., Corbel, B., and Delery, J., "Study of Passive Control in a Transonic Shock Wave/Boundary-Layer Interaction," *AIAA Journal*, Vol. 36, No. 3, 1998, pp. 394–400.

[6]Raghunathan, S., and Mabey, D., "Passive Shock-Wave/Boundary-Layer Control on a Wall-Mounted Model," *AIAA Journal*, Vol. 25, No. 2, 1987, pp. 275–278.

[7]Nagamatsu, H. T., Mitty, T. J., and Nyberg, G. A., "Passive Shock Wave/Boundary Layer Control of a Helicopter Rotor Airfoil in a Contoured Transonic Wind Tunnel," AIAA Paper 87-0438, Jan. 1987.

[8]Gefroh, D., Loth, E., Dutton, C., and McIlwain, S., "Control of an Oblique Shock/Boundary-Layer Interaction with Aeroelastic Mesoflaps," *AIAA Journal*, Vol. 40, No. 12, 2002, pp. 2456–2466.

[9]Hafenrichter, E. S., Lee, Y., McIlwain, S., Dutton, J. C., and Loth, E., "Experiments on Normal Shock/Boundary Layer Interaction Control Using Aeroelastic Mesoflaps," AIAA Paper 2001-0156, Jan. 2001.

[10]Hafenrichter, E. S., Lee, Y., Dutton, J. C., and Loth, E., "Normal Shock/Boundary Layer Interaction Control Using Aeroelastic Mesoflaps," *Journal of Propulsion and Power*, Vol. 19, No. 3, 2003, pp. 464–472.

[11]Lee, Y., Hafenrichter, E. S., Jaiman, R. K., Orphanides, M. J., Dutton, J. C., and Loth, E., "Skin Friction Measurements in Normal Shock Wave/Turbulent Boundary-Layer Interaction Control with Aeroelastic Mesoflaps," AIAA Paper 2002-0979, Jan. 2002.

[12]Inger, G. R., and Zee, S., "Transonic Shock Wave/Turbulent-Boundary-Layer Interaction with Suction or Blowing," *Journal of Aircraft*, Vol. 15, No. 11, 1978, pp. 750–754.

[13]Tanner, L. H., and Blows, L. G., "A Study of Motion of Oil Films on Surfaces in Air Flows with Application to the Measurement of Skin Friction," *Journal of Physics: Scientific Instruments*, Vol. 9, No. 3, 1976, pp. 194–202.

[14]Kim, K.-S., and Settles, G. S., "Skin Friction Measurements by Laser Interferometry in Swept Shock/Boundary-Layer Interactions," *AIAA Journal*, Vol. 28, No. 1, 1990, pp. 133–139.

[15]Garrison, T. J., "The Interaction Between Crossing-Shock Waves and a Turbulent Boundary-Layer," Ph.D. Dissertation, Dept. of Mechanical Engineering, Pennsylvania State Univ., University Park, PA, Aug. 1994.

[16]"Technical Data Sheet of Silicone Fluids 200," Dow–Corning Corp., Form 25-942-97, Midland, MI, 2000.

[17]Spalding, D. B., and Chi, S. W., "The Drag of a Compressible Turbulent Boundary Layer on a Smooth Flat Plate with and Without Heat Transfer," *Journal of Fluid Mechanics*, Vol. 18, 1964, pp. 117–143.

[18]Sun, C. C., and Childs, M. E., "A Modified Wall Wake Velocity Profile for Turbulent Compressible Boundary Layers," *Journal of Aircraft*, Vol. 10, 1973, pp. 381–383.

[19]Kooi, J. W., "Experiment on Transonic Shock-Wave/Boundary Layer Interactions," *AGARD Conference on Flow Separation*, CPP-168, AGARD, 1975.

[20]Hafenrichter, E. S., "Experiments on Normal Shock/Boundary Layer Interaction Control Using Aeroelastic Mesoflaps," M. S. Thesis, Dept. of Mechanical and Industrial Engineering, Univ. of Illinois, Urbana, IL, April 2001.

M. Sichel
Associate Editor